communications materials

A Nature Portfolio journal

Article

https://doi.org/10.1038/s43246-025-00865-5

Hydrogen sensing with high-performance via O^- ion spillover at Pd single atoms stabilized SnO_2 interface

Yunxiao Qian[1], Guorui Zhao[1], Changming Zhang[2], Shengjie Yin[1], Junwei Chen[1], Yuanyuan Luo[3], Zhengfeng Huang[1], Bo Liu[1] ✉ & Guotao Duan[2]

Developing hydrogen sensors with high performances is imperative for facilitating H_2-related industries. Metal oxide semiconductor (MOS) based gas sensors are simple structures with low cost that are a promising approach for H_2 detection. However, detection speed and selectivity of MOS-based sensors currently face great challenges. Herein, we design palladium single atoms (SAs) doped tin oxide (SnO_2/Pd_{atom}) for H_2 detection. Actual sensing tests show an ultrafast response speed toward H_2 (3s to 10 ppm H_2), with detection limit of 50 ppb and superior selectivity. Using in-situ THz time-domain spectroscopy and density functional theory calculations, it proves that an extra energy band near Fermi level appeared in SnO_2/Pd_{atom}, and Pd SAs doped on SnO_2 enhance signally concentration of free carrier in SnO_2/Pd_{atom}. Partial density of states reveals that coupling hybridization between Pd 4d orbital and O 2p orbital promotes electron injection from Pd 4d orbital into O π2p orbital, improving production of more O^- ions on sensing surfaces. Consequentially, the sensing dynamics involving O^- ions spillover at SnO_2-Pd_{atom} interface is discussed.

With the rapid development of industrialization, the issue of global warming is becoming more and more serious, caused mainly by greenhouse gas emissions such as carbon dioxide from the use of fossil fuels. For such a case, hydrogen (H_2), as a rich and low-carbon green energy source, has received great attention all over the globe because of its high combustion efficiency with water as the only byproduct[1–4]. However, owing to the easy escape of H_2 with colorless, odorless and its flammable and explosive nature[5,6], when the concentration of H_2 exceeds 4% in air, great safety accidents may occur during the use of H_2[7–9], such as the explosion of Norwegian H_2 fuel station, which was a dramatic obstruction for the development of H_2 related industry and economy. Therefore, considering safe use of H_2, high selectivity as well as fast detection for any H_2 leakage is of prime importance.

Gas sensors based on metal oxide semiconductors (MOS)[10–12] are one of the most widely used approaches for effectively detecting various hazardous gases due to their high sensitivity, fast response, low cost, easy integration, and so on. Specifically, in terms of H_2 detection, the performance requirements for gas sensors are more stringent, requesting an ultrafast response speed (<1 s) with high selectivity and a wide concentration range (0.1–10%), published by the U.S. Department of Energy[1,5,8,13]. However, up to now, there were no sensors to realize the above performance indicators for H_2 detection in practical application[14,15]. As for MOS-based sensors, although they could be used for H_2 leakage detection, the response time as well as selectivity have been facing great challenges. To improve both response time and selectivity of MOS-based sensors for H_2 detection, doping metal catalyst on the surfaces of pure MOS was regarded as a mainstream strategy. For example, Gaojie Li et al. used palladium nanoparticles (Pd NPs) to decorate tin oxide (SnO_2) ultrathin nanosheets, achieving enhanced response time (21 s toward 20 ppm H_2), which was shorter than that of neat SnO_2 nanosheets[16]. Moreover, Sihang Lu et al. functionalized SnO_2 nanowires with Pd NPs, producing excellent gas sensing properties for H_2 with a response time of 6 s[17]. Nevertheless, despite some improvements in performance have been made in H_2 detection via doping metal catalysts, most reports have mainly focused on simple performance regulation of metal catalysts on sensors, ignoring a very crucial factor of the inconsistent size and configuration of metal catalysts doped on MOS. Since the catalytic activity of metal particles is strongly dependent on their size and structure[18,19], thus the coexistence of metal particles with various sizes or structures, which occurred during the doping process of metal catalysts on MOS, may result in adverse impacts on sensing characteristics, especially selectivity and response time. Therefore, MOS-based gas sensors doped by metal catalysts still fall short of tough performance requirements for H_2 detection.

[1]School of Microelectronics, Hefei University of Technology, Hefei, PR China. [2]School of Integrated Circuits, Huazhong University of Science and Technology, Wuhan, PR China. [3]Key Lab of Materials Physics, Anhui Key Lab of Nanomaterials and Nanotechnology, Institute of Solid State Physics, Chinese Academy of Science, Hefei, PR China. ✉e-mail: 2021800194@hfut.edu.cn

To tackle such limitations, the key challenge is how to maintain consistency in size and construction of metal catalysts doped on MOS. Single-atom (SA) catalysts are an excellent alternative strategy for replacing metal particles, mainly due to their highly consistent dimensions and configuration with the maximum atom utilization efficiency[20–24]. In this regard, attempts have been made to tune the performance of MOS-based gas sensors by doping SAs. For instance, our group has adopted Pd SAs to modulate the performance of indium oxide-based gas sensors, proving that Pd SAs doped on indium oxide promoted dramatically detection ability to H_2S with a higher sensitivity and selectivity compared to the doped Pd NPs[20]. Moreover, Cu SAs stabilized WO_3 nanowires, developed by Huan Liu and co-workers, were used as a sensing layer for toluene detection, showing a higher sensitivity with faster detection speed in contrast with the decoration of Cu NPs[25]. These results indicate an advantage of metal SAs for promoting the performance of MOS-based gas sensors, which is more suitable than corresponding metal particles. However, although SAs doped on MOS have exhibited a better potential for optimizing gas sensing performances, the current application in facilitating the performance of H_2 detection is still relatively limited. Furthermore, the underlying mechanism by which SAs regulate the properties of MOS gas sensors is unclear.

Herein, we primarily designed Pd SA-doped SnO_2 (SnO_2/Pd_{atom}) materials for improving detection properties to H_2 gas, achieving an ultrafast response speed to H_2 (3s to 10 ppm), with a detection limit of 50 ppb and outstanding selectivity. Density functional theory (DFT) calculations confirmed that interface between Pd SAs and SnO_2 (SnO_2–Pd_{atom} interface) in SnO_2/Pd_{atom} structure was an optimal active site, which showed the lowest adsorption energy (E_{ads}) to H_2, but the highest electron transfer with H_2 gas, indicating that it strengthened H_2 adsorption and promoted electron transfer from H_2 to sensing materials. In addition, through DFT calculations of energy band structure diagrams, it was found that an extra energy band originating from Pd SAs appeared near the Fermi level in SnO_2/Pd_{atom} materials. Particularly, partial density of states (PDOS) revealed a strong coupling hybridization between Pd 4 d orbital and O 2p orbital near the Fermi level, which was helpful for the activation and dissociation of the O=O bond of oxygen molecules adsorbed on SnO_2/Pd_{atom} materials. More significantly, an increase of free carriers in SnO_2/Pd_{atom} was determined by in-situ THz time domain spectroscopy (THz TDS), improving the production of more O^- ions on surfaces of SnO_2/Pd_{atom} material, which was further demonstrated by XPS test. On the basis of the above results, the sensing dynamics mechanism related to O^- ions spillover at the SnO_2–Pd_{atom} interface caused by coupling of Pd 4d orbital with O 2p orbital was proposed. As a consequence, a wireless H_2-sensing module based on such SnO_2/Pd_{atom} sensors was developed to verify its practical detection effect.

Results and discussion

The operation procedure for generation of Pd SA-doped SnO_2 configuration was presented in Fig. 1a. Originally, SnO_2 materials, with around 300 nm spherical diameter (Supplementary Fig. 1a) and porous hollow structure (Supplementary Fig. 1b), enabled to provide a larger impregnation space for Pd precursors, which would promote the effective deposition between Pd precursor species and SnO_2 supports. Moreover, as-prepared SnO_2 showed the nature of negative surface charges with an average potential value of around −20.67 mV (Supplementary Table 1), which helped to the adsorption of positively charged Pd-containing precursors to SnO_2 surfaces driven by electrostatic adsorption force (Supplementary Table 1), allowing the subsequent in-situ formation of Pd SAs. Processed by a high temperature in air, the anchored Pd cationic precursors were further transformed into Pd SAs and dispersed steadily on SnO_2.

As shown in Fig. 1b and Supplementary Fig. 1c, any structural information of Pd species was not observed from conventional transmission scanning electron microscopy (TEM) measurements, whether it was small Pd NPs or large PdO aggregates; only the hollow structure of SnO_2 was revealed clearly (Supplementary Fig. 1c). To prove the presence of Pd species, the ICP-MS measurement for such a sample was preliminarily carried out. According to the ICP-MS testing result, the loading amount of Pd was calculated to be 0.12 wt% in the as-prepared sample (with respect to SnO_2), which was close to the theoretical feeding ratio (0.15 wt%). It means that the as-synthesized samples did contain Pd species. In such a case, the X-ray diffraction (XRD) method was used to trace the crystalline phase of such a sample. However, besides the main characteristic peaks that derived from tetragonal SnO_2 (JCPDS 96-100-0063) (Supplementary Fig. 2), there was no unambiguous identification of diffraction peaks that originated from Pd species from the XRD pattern, whether Pd NPs or PdO particles, which was consistent with the results of TEM-SAED (Supplementary Fig. 3). Based on these results, it is speculated that as-formed Pd species on samples may be atomically dispersed. To validate this viewpoint, the objective lens spherical-aberration correction TEM (SAC-TEM) testing was also performed. As revealed in Fig. 1c, d, it is obvious that only Pd species with atomic dispersion were recognized at different areas (red circles), without any trail of Pd particles or aggregates, proving that Pd species maintained on SnO_2 were single atoms. Meanwhile, through the energy dispersive X-ray spectrometry (EDS) map scanning, it was found that the formed atomic Pd species were distributed uniformly over SnO_2 (Supplementary Fig. 1d). Comparatively, with the increase of the initial dosage of Pd precursors in SnO_2 dispersion, following by reduction with a reducing agent, as shown in Supplementary Fig. 4, it is observed that Pd NPs with a size of around 5 nm (Supplementary Fig. 4c) easily formed and distributed equally on SnO_2 surfaces (Supplementary Fig. 4d–f). It suggests that cationic Pd precursors are able to be easily anchored uniformly to SnO_2 surfaces, which offers a guarantee for the fabrication of Pd SAs using a small dosage of Pd precursors.

Additionally, X-ray absorption spectroscopy (XAS) measurements were utilized to analyze deeply the nature of Pd species formed on SnO_2. X-ray absorption near edge structure (XANES) spectra of Pd *K*-edge offered evident information that the position of the white line for Pd species in SnO_2/Pd_{atom} samples shifted to a higher energy region compared with Pd foil, and moved to a lower energy area in comparison to PdO reference. It confirmed that the atomically dispersed Pd species was cationic, with an oxidation state between +2 and 0[26,27]. Moreover, the surface composition and chemical state of the as-prepared SnO_2/Pd_{atom} sample were also investigated by X-ray photoelectron spectroscopy (XPS) measurements. As shown in Supplementary Fig. 5b, two characteristic peaks of 495.05 and 486.55 eV appeared, which are attributed to Sn $3d_{5/2}$ and Sn $3d_{3/2}$, respectively[28]. In addition, other obvious peaks located at 530.60 and 531.42 eV were also observed (Supplementary Fig. 5c), which originated from O 1s[29]. Significantly, it was clear that the peaks of 336.97 and 342.19 eV were exhibited in Supplementary Fig. 5d, which derived from Pd $3d_{5/2}$ and Pd $3d_{3/2}$, respectively. However, it is noticed that these two peaks are less than those of Pd divalent cation in as-prepared SnO_2/PdO samples (342.49 eV and 337.12 eV for Pd $3d_{3/2}$ and Pd $3d_{5/2}$[30], respectively) (Supplementary Fig. 6a), but higher than those of Pd zero valence in as-synthesized SnO_2/Pd_{nano} samples (340.59 eV and 335.28 eV for Pd $3d_{3/2}$ and Pd $3d_{5/2}$[16], respectively) (Supplementary Fig. 6c). Such results were in keeping with those of XANES spectra, reflecting that atomically dispersed Pd species doped on SnO_2 showed a positively charged valence state that between positive divalent and zero valence.

Also, as far as SnO_2/Pd_{atom} samples, in the quantitative least-square extended X-ray absorption fine structure (EXAFS) fitting data for *K*-space (Fig. 1f and Supplementary Fig. 7a), it showed an apparent absence of the strongest oscillation signal in the high *K* area initiated by metal action, indicating that the coordination configuration consisted of metal-light element, governed in this sample. Furthermore, the Fourier transformed *R*-space analysis of EXAFS spectra revealed that an obvious peak located at 1.53 Å, originating from Pd–O scattering feature, appeared for SnO_2/Pd_{atom} samples (Fig. 1g and Supplementary Fig. 7b). Notice that there was no evidence of Pd–Pd bonds observed in such samples, which was distinct from that in Pd foil. Thus, it displayed that the coordination structure of Pd–O bonds was dominant in synthesized SnO_2/Pd_{atom} samples, without a prominent signal of Pd cluster or particles caused by metal aggregation, which matched with that of the quantitative least-square EXAFS analysis, meaning

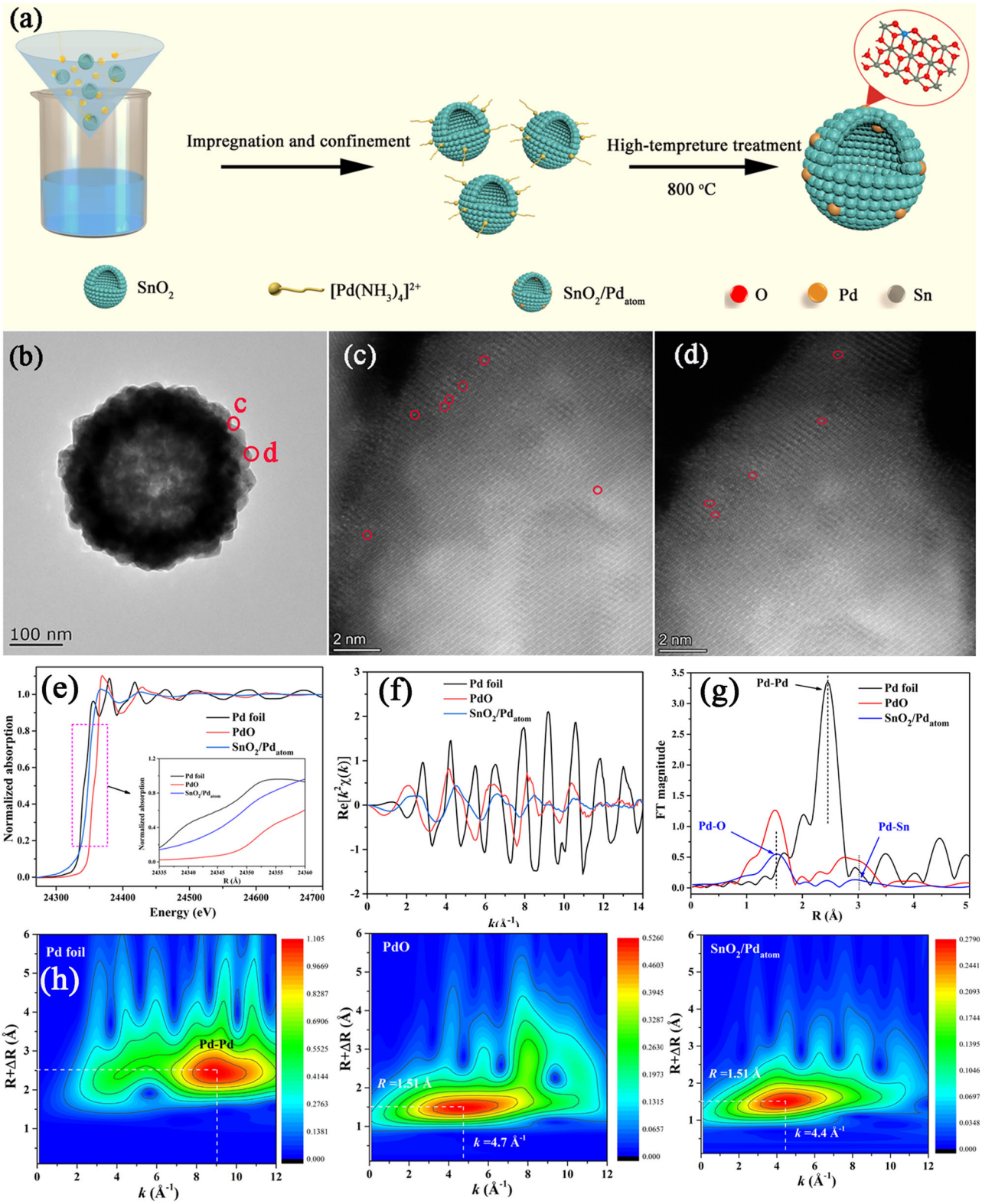

Fig. 1 | Morphological, structural, and compositional characterization of SnO_2/Pd_{atom}. **a** The schematic diagram of prepared Pd SA-doped SnO_2 (SnO_2/Pd_{atom}) materials, **b** the low-resolution TEM image of the prepared SnO_2/Pd_{atom} samples and **c**, **d** the corresponding spherical-aberration TEM images at different areas, **e** the normalized XANES spectra at Pd K-edge (inset: expansion of the highlighted pink area) and **f** the transformed k-space curve and **g** the corresponding Fourier transformed k^2-weighted $\chi(k)$ function of k^2-weighted EXAFS spectra and **h** Wavelet transformation (WT) EXAFS for Pd foil, PdO reference and as-synthesized SnO_2/Pd_{atom} samples.

that no Pd clusters or particles were generated in such samples. Moreover, in contrast with the PdO reference, the intensity of Pd–O bands was dramatically weaker, which was probably induced by a certain distortion near the formed Pd atoms[20,31,32]. The fitting of EXAFS data showed that, excepting for the first-shell Pd–O coordination with an average bond length of 2.14 Å that matched well with the proposed theoretical model (Supplementary Table 2 and Supplementary Fig. 8), a weak second-shell signal at around 3.16 Å with a coordination number of 1.2 ± 0.1 (Supplementary Fig. 7b and Supplementary Table 2) also occurred in SnO_2/Pd_{atom} samples, differing from the second-shell Pd–Pd distance in PdO refs. 20,33, which can be attributed to Pd-Sn bonds. More importantly, the wavelet transformed (WT) analysis of Pd *K*-edge EXAFS data for SnO_2/Pd_{atom} samples revealed that only the strongest peak at 4.4 $Å^{-1}$ and 1.51 Å in *K*-space and *R*-space, respectively, was seen (Fig. 1h), which was ascribed to Pd–O bond scattering. Nevertheless, it is worth noting that there was no signal of metallic Pd–Pd coordination, demonstrating the absence of Pd clusters or particles in SnO_2/Pd_{atom} samples. Therefore, according to the above analysis, it is concluded that Pd species doped in SnO_2 were indeed atomically dispersion, and these Pd atoms are distributed in different regions of SnO_2 material in the form of a single atom.

The H_2 detection performances of sensors based on SnO_2/Pd_{atom} materials

In terms of H_2 detection using SMOs-based gas sensors, most research was currently either based on pure SMOs or SMOs doped with metal nanocatalysts. However, there are few reports on H_2 detection by doping single atomic catalysts. For such a case, theoretical calculations are primarily performed to predict whether the doping of Pd SAs can facilitate the detection of H_2 gas molecules. As shown in Supplementary Fig. 9, on the basis of XRD results, the theoretical model for Pd SA-doped SnO_2 and pure SnO_2, respectively, was optimized and established. Given that electron transfer and surface reaction mainly contributed to gas sensing properties[34,35], we originally tracked if there was an optimal active site for H_2 adsorption on surfaces of SnO_2/Pd_{atom} material. With regard to surfaces of SnO_2/Pd_{atom} material, four different active sites that may affect the adsorption of H_2 gas molecules were initially estimated, those are the interaction region between single Pd atoms and adjacent O atoms without forming covalent bonds (defined as the SnO_2–Pd_{atom} interface), Pd atom site (SnO_2–Pd_{atom}–Pd site), O sites (SnO_2–Pd_{atom}–O site) and Sn sites (SnO_2–Pd_{atom}–Sn site). As revealed in Fig. 2a and Supplementary Fig. 10, when H_2 gas molecules were adsorbed to the SnO_2–Pd_{atom} interface site, its adsorption energy (E_{ads} = −2.01 eV) was much lower than those on other different sites (E_{ads} = −0.43 eV, −0.18 eV, −0.20 eV for Pd atom site, O site and Sn site, respectively), indicating that the SnO_2–Pd_{atom} interface site owned the strongest adsorption capacity toward H_2 and could be regarded as the best adsorption site.

Furthermore, as a comparison, for both O sites and Sn sites on neat SnO_2, it exhibited very small adsorption to H_2 gas molecules (E_{ads} = −0.04 eV and −0.19 eV for O site and Sn site, respectively) (Supplementary Figs. 11, 12), meaning that the doping of Pd SAs could polish up the adsorption ability of SnO_2 to H_2 to a large extent. The theoretical electron transfer was also traced. According to DFT results, as displayed in Fig. 2b, for above-mentioned four diverse sites in SnO_2/Pd_{atom}, it found that H_2 molecules adsorbed on the SnO_2–Pd_{atom} interface would lose 0.73 e, which was much than those on other sites (the quantity of electron transfer from H_2 to SnO_2–Pd_{atom}–Pd site, SnO_2-Pd_{atom}-O site, SnO_2-Pd_{atom}-O site was 0.19, 0.03, 0.03, respectively). It further implied that Pd SAs doped on SnO_2 were able to improve activation for H_2. Thus, based on such calculation results, it is speculated that the SnO_2–Pd_{atom} interface will be the best adsorption and activation position for H_2 molecules, which may bring about an outstanding H_2-sensing signal.

Additionally, as for the SnO_2–Pd_{atom} interface site, we also calculated its adsorption and activation ability for other different gases. As revealed in Fig. 2c, the E_{ads} for other diverse gas molecules adsorbed on the SnO_2–Pd_{atom} interface were much higher than that for H_2 molecules, confirming its excellent selective adsorption to H_2 gas. Moreover, the amount of electron transfer between the SnO_2–Pd_{atom} interface and other various gas molecules (including HCHO, NH_3, CH_4, CO_2, NO_2) was very small, with 0.21 e, 0.28 e, 0.12 e, 0.07e, 0.14 e, respectively (Fig. 2d and Supplementary Fig. 13). Obviously, they were much smaller than that with H_2 molecules, illustrating that such active site has a higher advantage in activating H_2 in comparison to other interfering gases, which theoretically supports the possibility that produces highly selective signal for detecting H_2 gas.

In order to validate DFT calculation results, the actual sensing tests for SnO_2/Pd_{atom}-based sensors toward H_2 were conducted. Initially, the optimum working temperature of such a sensor was estimated, as shown in Fig. 3a and Supplementary Fig. 14a, it was evident that the highest gas response was obtained for 10 ppm H_2 when the working temperature was 170 °C, indicating its optimum working temperature was 170 °C. Furthermore, as a comparison, it also found that two other types of sensors, which based on neat SnO_2 and SnO_2/PdO, respectively, exhibited higher optimal operating temperatures but lower gas response value toward the same concentration of H_2, meaning that Pd SAs-doping has a promoting effect on both working temperature and gas response value. Hence, the subsequent sensing performance indicators were carried out at 170 °C. In addition, the relationship between response time and working temperature of sensors was further traced (Supplementary Fig. 14b). With increasing working temperature, the response time for SnO_2/Pd_{atom}-based sensors decreased greatly. But after the working temperature exceeds 170 °C, the response time for such sensors hardly changes. In comparison, although the overall trend of this relationship for the other three sensors was almost consistent with that of the SnO_2/Pd_{atom}-based sensor, the response time for the SnO_2/Pd_{atom}-based sensor was shorter than that for the other three sensors.

Also, the response time as well as recovery time was compared for such four types of sensors (neat SnO_2, SnO_2/PdO, SnO_2/Pd_{atom}, and SnO_2/Pd_{nano}). As far as the SnO_2/Pd_{atom}-based sensor was concerned, its response speed was very fast, with the time of 3 s to 10 ppm H_2, but the recovery speed was relatively slow (Supplementary Fig. 15b). However, among above four different sensors, both response and recovery time of the SnO_2/Pd_{atom}-based sensor are the shortest toward H_2 gas at a wide range of concentrations (Fig. 3b, c). It means that Pd SAs doped on SnO_2 are capable of greatly boosting the response/recovery speed of sensors, especially at low concentration of H_2 gas (<5 ppm), where their response speed can be increased by about an order of magnitude in contrast with sensors based on neat SnO_2 (Fig. 3b).

Additionally, the detection limit for SnO_2/Pd_{atom}-based sensors was further assessed. As revealed in Fig. 3d, e (blue line), the resistance of such a sensor decreased as the concentration of H_2 increased, and the corresponding gas response value gradually reduced with the decrease of H_2 concentration. Until the concentration dropped to 50 ppb, it still showed a certain response value (Fig. 3g, h). However, when H_2 concentration was less than 50 ppb, no gas response signal appeared (Supplementary Fig. 15a), proving that the detection limit of such a sensor toward H_2 can reach 50 ppb. Importantly, in comparison to SnO_2 doped with Pd NPs or PdO particles, the introduction of Pd SAs yielded a greater improvement in both gas response value and detection limit of H_2 gas (Fig. 3e, h), which was close to the prediction of DFT calculations.

As exhibited in Fig. 3f, for a pure SnO_2-based sensor, the relationship between gas response value and concentration of H_2 was linear (black fitting curve). However, as for the SnO_2/Pd_{atom}-based sensor, the correlation between gas response value and H_2 concentration was nonlinear (blue fitting curve). It indicated that the doping of Pd SAs might alter the H_2 sensing mechanism of SnO_2 materials. Replacing data fitting across the entire H_2 concentration range, if such data was fitted in stages (Supplementary Fig. 16), two different linear correlations were shown for low (≤10 ppm) and high (≥10 ppm) concentration of H_2 gas, respectively. It will help promote quantitative H_2 concentration detection. Moreover, due to the slope of fitting curve between gas response value and gas concentration can be regarded to estimate the sensitivity of sensors[36], the sensitivity of the SnO_2/

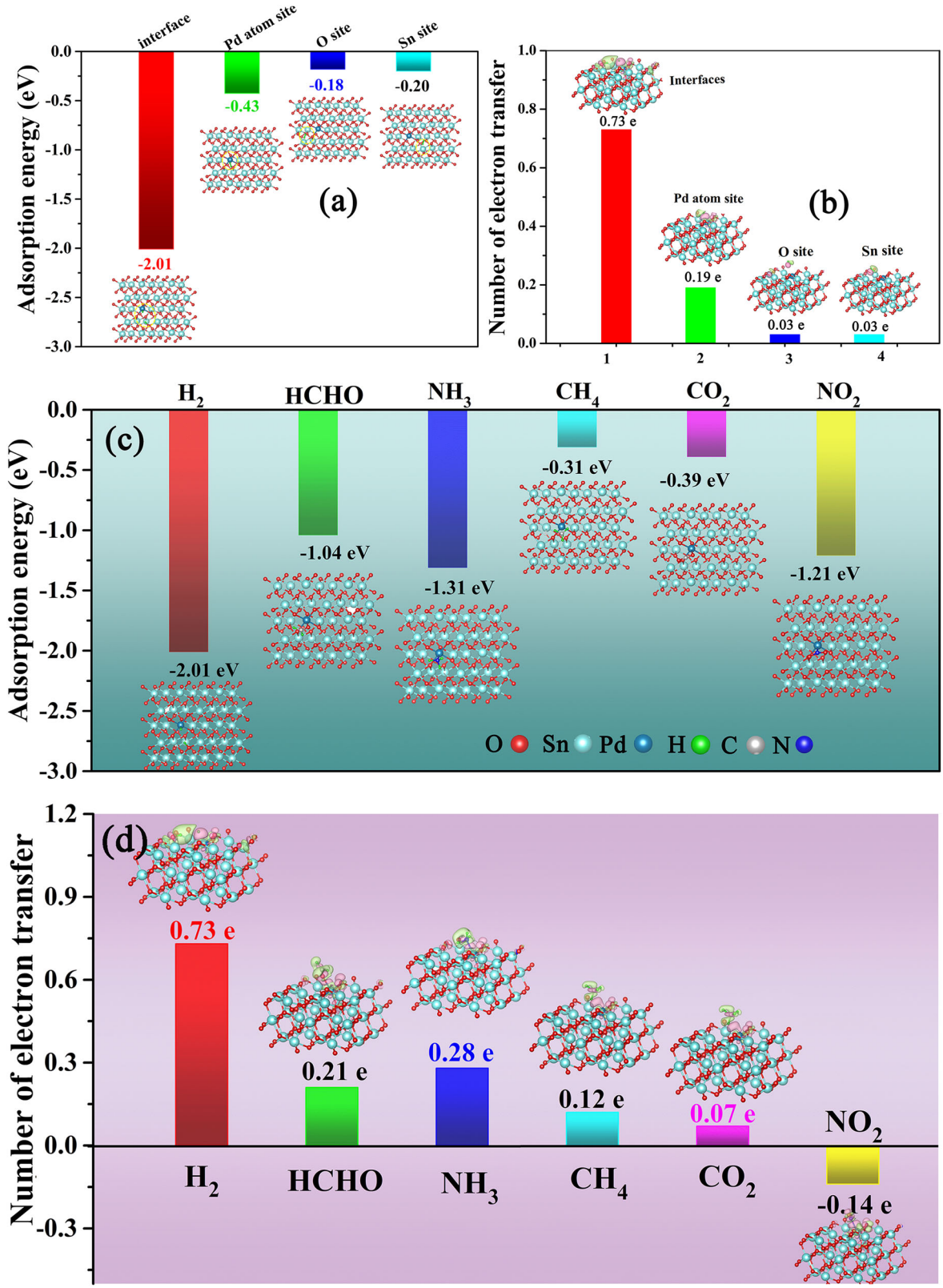

Fig. 2 | Adsorption energy and bader charge of H_2 gas adsorbed on different sites of SnO_2/Pd_{atom}. **a** The adsorption energy (E_{ads}) variation of H_2 gas molecules adsorbed on different active sites of SnO_2/Pd_{atom}. **b** Bader charge (Δq) of H_2 gas molecules adsorbed on different active sites of as-prepared SnO_2/Pd_{atom} surfaces, **c** the E_{ads} comparison, and **d** Bader charge (Δq) comparison of different gas molecules (H_2, HCHO, NH_3, CH_4, CO_2, NO_2) adsorbed on SnO_2–Pd_{atom} boundary.

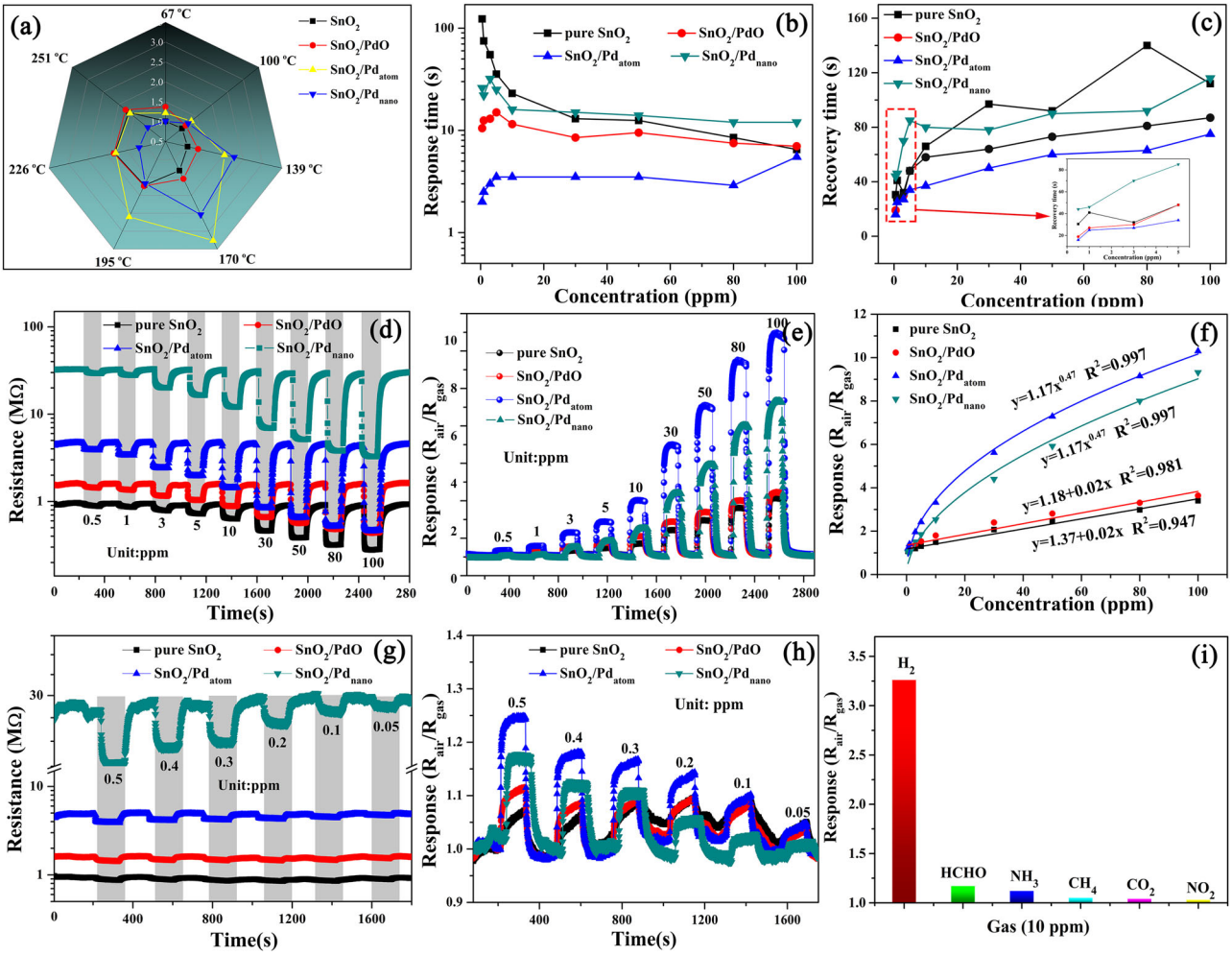

Fig. 3 | Sensing performances of SnO_2/Pd_{atom} based sensor to H_2 gas. a The relation between gas response and working temperature toward 10 ppm H_2 for sensors based pure SnO_2, SnO_2/PdO, SnO_2/Pd_{atom} and SnO_2/Pd_{nano}, respectively, **b** response time comparison, and **c** recovery time comparison toward a range concentration of H_2 from 0.5–100 ppm for above four different sensors, **d** the dynamic resistance change, and **e** the corresponding response value variation and **f** the corresponding relation curve between H_2 gas concentration and gas response value at wide concentration range for H_2 gas sensing of SnO_2/Pd_{atom}-based sensors contrasted with reference sensors at 170 °C, **g** the dynamic resistance change and **h** the corresponding response value variation at low concentration range for the H_2-sensing property of SnO_2/Pd_{atom}-based sensors contrasted with reference sensors at 170 °C, **i** the selectivity evaluation of SnO_2/Pd_{atom}-based sensors to H_2 gas at 170 °C.

Pd_{atom}-based sensor toward H_2 with low concentration (the slop is 0.22 ppm^{-1}) was higher than that with high concentration (the slop is 0.07 ppm^{-1}). As for such a fitting characteristic, it is supposed that the Langmuir adsorption isotherm theory of dissociated gas and the available surface sites on Pd SA-doped SnO_2 materials may be reasons for it.

Besides, during five consecutive cycles of testing for such sensors (Supplementary Fig. 15c), it was obvious that the gas response value of such SnO_2/Pd_{atom}-based sensors toward 5 ppm H_2 had almost no change, and the baseline for every cycle of testing also showed almost no significant difference, meaning its superior reusability. Furthermore, during five consecutive injections of 100 ppb H_2 in a testing chamber without a recovery process, the resistance variation of such a sensor showed a distinguishable stepped lowering pattern (Supplementary Fig. 15d), indicating that it possessed an excellent low concentration sensitivity. The humidity resistance of SMO-based gas sensors was an important performance indicator; thus, the influence of relative humidity on the gas response of such sensors was measured. As exhibited in Supplementary Fig. 15e, as relative humidity increased, the gas response of the SnO_2/Pd_{atom}-based sensor to 10 ppm H_2 significantly decreased, implying its poor humidity resistance, which may be caused by the competitive adsorption between H_2O molecules and H_2 on the surfaces of this sensor[37,38]. For such a case, in order to decrease the impact of humidity on sensors, the breathable and hydrophobic coating[39,40], which covers the surface of the sensing materials layer, is a very effective and commonly used approach. In our study, considering minimizing the impact of coating on sensing performances of sensors as much as possible, the breathable and hydrophobic fluoropolymer coating, such as Teflon AF-2400 with the high gas permeability and chemical stability[40], can be chosen as protective coatings to cover SnO_2/Pd_{atom} sensing layer for improving its anti-humidity. This part of the research will be systematically studied in the future. The long-term stability was also crucial for the practical applications of sensors. During fifteen days of gas detection test, it was found that the gas response value of such sensor toward 10 ppm H_2 revealed very small variations (Supplementary Fig. 15f), indicating that SnO_2/Pd_{atom}-based sensors had a better long-term stability.

The theoretical calculations of E_{ads} above-mentioned have shown that SnO_2–Pd_{atom} interfaces, which exist on the surface of the sensing layer, have the strongest adsorption to H_2 compared to other gases; thereby, it is speculated that a greatly selective detection signal to H_2 gas may be yielded. Accordingly, the selective detection measurement for SnO_2/Pd_{atom}-based sensors was carried out. As displayed in Fig. 3i, in accordance with the gas types involved in the theoretical calculations, under the same gas concentration, it is obvious that such sensors showed almost no gas response to CH_4, CO_2, and NO_2. Moreover, while a very small sensing response appeared for HCHO and NH_3 (1.17 and 1.12 for HCHO and NH_3,

respectively), the gas response of such sensors to the same concentration of H_2 was much higher. Through the comparison of gas response, it did demonstrate that the SnO_2/Pd_{atom}-based sensor has an excellent selectivity for H_2 detection. For such a case, it may be attributed to the enhanced adsorption capacity and greater reactivity of H_2 molecules on the surface of Pd SA-doped SnO_2 materials[9,41]. In fact, the selectivity of such sensors was well matched with the results of DFT calculations. As discussed above in Fig. 2c, d, the E_{ads} for H_2 on the surface of Pd SA-doped SnO_2 were far less than those for other interfering gases, confirming that the surface of Pd SA-doped SnO_2 had an excellent selective adsorption ability for H_2. Meanwhile, the amount of electron transfer between the SnO_2/Pd_{atom} interface and H_2 was much higher than that of other interfering gases, demonstrating that the surface of SnO_2/Pd_{atom} materials had greater reactivity to H_2 molecules. Hence, these two factors may be reasons for such superior selectivity of Pd SA-doped SnO_2 toward H_2.

As a comparison, a pure SnO_2-based sensor showed very poor response to either interfering gases or H_2, evidencing its poor selectivity for H_2 detection. It is worth noting that although Pd NPs or PdO particles were introduced onto SnO_2, such a prominently selective detection signal to H_2 was not observed (Supplementary Fig. 17, blue and green bar chart). Following these comparisons, it confirms that Pd SAs doped on SnO_2 can markedly improve selectivity and sensing response to H_2 gas, but also indicates that such performance improvement caused by Pd-SAs doping is notably better than those of doped Pd NPs or PdO particles.

Currently, there have been many reports on MOS-based sensors that are used to detect H_2 gas. In order to reflect the merits of Pd SAs-doping in promoting the performance of H_2 sensors, an overall performance comparison was made. As exhibited in Supplementary Table 3, it is found that most of references showed higher working temperature compared with our work, excepting for ref. 11 in Supplementary Table 3. Additionally, it was noticed that response time and detection limit of SnO_2 sensor doped with Pd SAs toward H_2 gas were shortest in comparison with other published state-of-the-art materials in Supplementary Table 3, excepting for the detection limit in ref. 1. But it must point out that the gas response value of such sensor was lower than other reports. Generally, through the above comparisons, it implies that doping Pd SAs into SMO-based sensors can provide an effective approach to improve sensing properties for H_2 detection.

The sensing mechanism of SnO_2/Pd_{atom}-based sensors to H_2 gas

As for the gas sensing mechanism of SMOs doped with metal NPs, it usually involves oxygen spill-over[42–44] or Fermi-level modulation[34,45]. Accordingly, the impact of doped Pd SAs on the band structure of SnO_2 materials was preliminarily studied by DFT calculations. As revealed in Fig. 4a, b, compared with pure SnO_2 (Fig. 4a), when Pd SAs were introduced to SnO_2, it is apparent that an extra band near the Fermi level emerged on the conduction band side (Fig. 4b), suggesting the generation of a new impurity level in the band configuration of SnO_2/Pd_{atom}, which is possibly induced by the doped Pd SAs. Specifically, according to the band theory of semiconductors[46], the presence of an impurity level is conducive to a lower barrier of electron transition, where the transition of electrons will start from the valence band to the impurity level, and then to the conduction band (Supplementary Fig. 20a, b). It makes electron transition easier under the same excitation conditions, which can significantly increase carrier concentration in the conduction band. More importantly, calculations of partial density of states (PDOS) showed a clear overlap between 4d orbital of Pd atoms and 2p orbital of O atoms in SnO_2/Pd_{atom} samples (red box in Fig. 4c and Supplementary Fig. 18), which was not observed in that of pure SnO_2 (Fig. 4d). Obviously, such overlapping peak is very close to Fermi level (red circle in Supplementary Fig. 18), which means that the energy of bonding orbitals between Pd atom and O atom is relatively high, enabling to formation of Pd–O bond and promoting electron injection from 4d orbital of Pd atom into π 2p orbital of O atom. In order to verify the formation of the Pd–O bond, the in-situ Raman spectroscopy was carried out.

As shown in Supplementary Fig. 19, at the working temperature of SnO_2/Pd_{atom}-based sensors (170 °C), when the SnO_2/Pd_{atom} materials was not in contact with H_2, excepting for three fundamental Rama active peaks at 471, 628 and 766 cm^{-1}, which was attributed to vibrational mode of E_g, A_{1g} and B_{2g} of the rutile tetragonal structure SnO_2[47,48]. A Raman peak of 405 cm^{-1} was also emerged, which was associated with the E_g vibrational modes of PdO[48,49], indicating the formation of the Pd–O bond. Specially, once the SnO_2/Pd_{atom} materials was exposed in 100 ppm H_2 at 170 °C, it was found that the Raman peak of Pd–O vibrational mode was weaker compared to the absence of H_2, demonstrating the orbital hybridization between Pd atom and O atom, and Pd–O bond played an important role in such an H_2-sensing process. Therefore, it is more beneficial for the activation of the O=O bond for the adsorbed oxygen molecules[50,51], increasing the amount of adsorbed oxygen species on the surfaces of SnO_2/Pd_{atom} samples.

To determine the results of DFT calculations through experiments, the terahertz time domain spectroscopy (THz TDS) measurements for these two samples were implemented. As revealed in Supplementary Fig. 18c, d, under in-situ heating to 170 °C for SnO_2/Pd_{atom} and pure SnO_2 film loaded on quartz substrate, respectively, which matched with the working temperature of SnO_2/Pd_{atom}-based sensors. Primarily, the transmitted THz electric field waveform through a substrate was detected, and the electric strength is E_{sub}. Then, the THz electric strength of the transmitted THz electric field waveform through pure SnO_2 and SnO_2/Pd_{atom} is E_{SnO2} and $E_{SnO2/Pdatom}$, respectively. Compared to pure SnO_2, the peak of THz electric field intensity decreased after passing through the SnO_2/Pd_{atom} (Supplementary Fig. 20c, d), indicating a remarkable absorption of the THz waveform induced by free carriers. Moreover, the optical conductivity of pure SnO_2 and SnO_2/Pd_{atom} can be achieved based on following equation[52]:

$$\frac{E_{sample+sustrate}(\omega)}{E_{sample}(\omega)} = \frac{1+n}{1+n+Z_0\sigma(\omega)}$$

Herein, n represents refractive index of the substrate, Z_0 is impedance of the free-space (≈377), and $\sigma(\omega) = \sigma_1(\omega) + i\sigma_2(\omega)$ is complex optical conductivity with ω being the photon frequency[52]. THz TDS here measured mainly the optical response of free carriers within the sample. As shown in Fig. 4e, f, the frequency domain optical conductivity of neat SnO_2 and SnO_2/Pd_{atom}, respectively, is obtained by using the fast Fourier transform. The solid lines are fitting lines by applying a Drude Model[53]. It is calculated that the carrier density in pure SnO_2 and SnO_2/Pd_{atom} is about $1.9*10^{14}$ cm^{-2} and $2.7*10^{14}$ cm^{-2}, respectively, which certifies a prominent increase of carrier population in SnO_2/Pd_{atom} in comparison to neat SnO_2. Such experimental results are parallel to those of DFT calculations, confirming that Pd SAs doped in SnO_2 do indeed increase the concentration of free carriers.

Additionally, the amount of surface-adsorbed oxygen species on these two samples was also traced by XPS measurements. According to a previous report, the chemisorbed oxygen species were predominantly as O^- ions on surfaces of metal oxides between 420 and 670 K[54]. In this work, since the working temperature of sensors based on SnO_2/Pd_{atom} was 170 °C (about 444 K), the quantity of chemisorbed O^- ions on the surfaces of sensing materials was mainly investigated. As shown in Supplementary Fig. 20d, e, these two sensors were primarily heated to 170 °C in air, respectively, and then cooled immediately to room temperature for XPS measurements. It is observed that the quantity of O^- ions on surfaces of SnO_2/Pd_{atom} sensing materials was about 23.63% (Supplementary Fig. 20e), much higher than that (19.36%) of neat SnO_2 (Supplementary Fig. 20d), proving that Pd SAs doped on SnO_2 promoted the adsorption and dissociation of oxygen molecules, which was in good agreement with results of DFT calculation (Fig. 4c, d).

Therefore, combing DFT calculations with experimental measurements, a sensing mechanism for SnO_2/Pd_{atom}-based sensors toward H_2 was put forward: as revealed in Fig. 4g, when such sensor was exposed in air, due to the doping of Pd SAs in SnO_2, the new impurity level was formed in band configuration of SnO_2/Pd_{atom}, which reduced the barrier of electron transition from valance band to conduction band, causing a great enhancement of electron concentration in SnO_2/Pd_{atom} materials. Meanwhile, by means

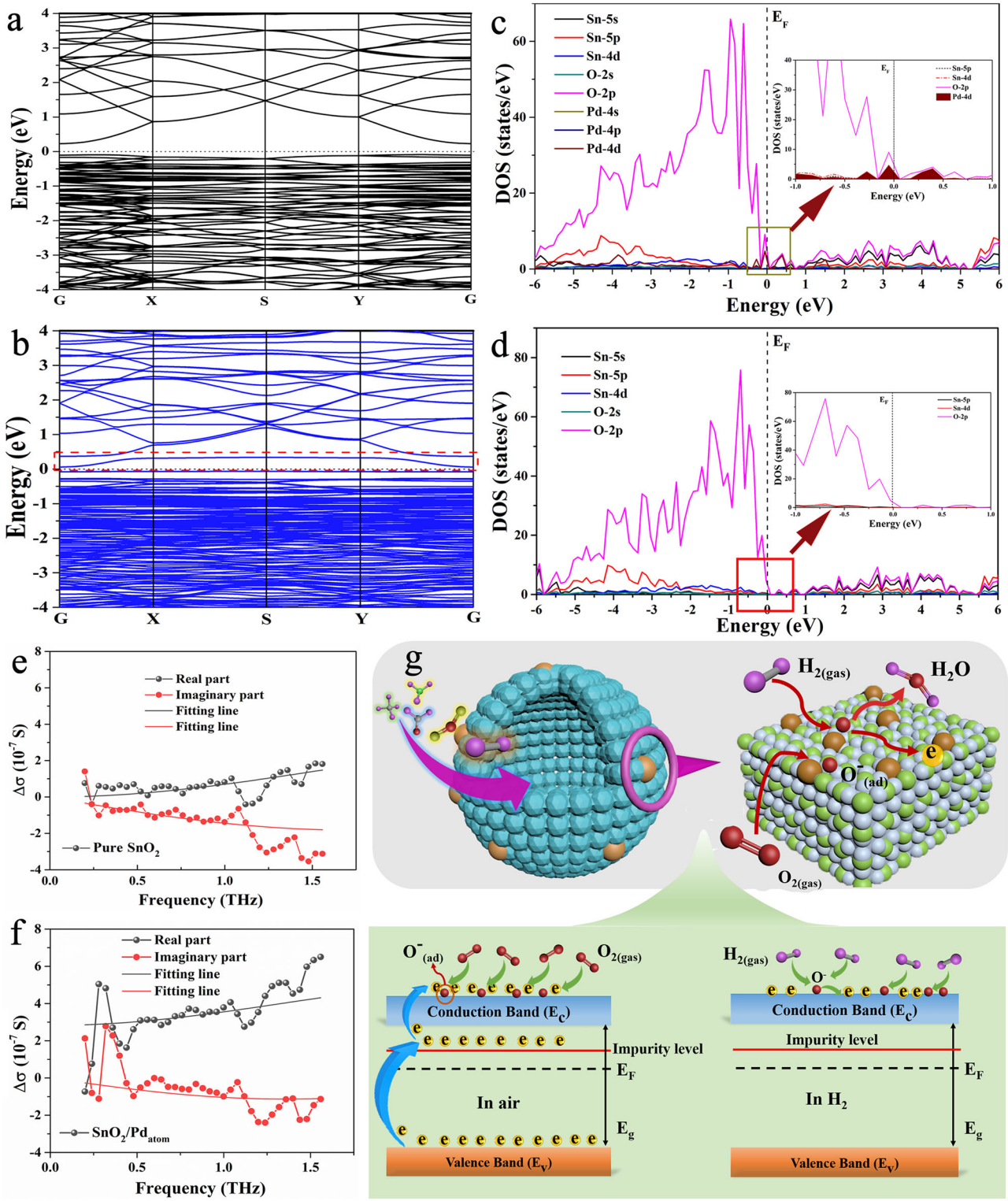

Fig. 4 | Theoretical energy band structure and partial density of satates calculations for SnO_2/Pd_{atom}. The calculated energy band structure diagrams of **a** pure SnO_2 and **b** as-prepared SnO_2/Pd_{atom} based on DFT calculation. The partial density of states (PDOS) for **c** as-prepared SnO_2/Pd_{atom}, and **d** pure SnO_2 based on DFT calculation. The Fourier transformed frequency-resolved complex conductivity from the THZ time domain spectroscopy of **e** pure SnO_2 and **f** as-prepared SnO_2/Pd_{atom}, whose symbols show experimental real (gray solid spheres) and imaginary (red solid circles) conductivities, the solid lines correspond to the fittings with Drude–Smith models. **g** The as-proposed H_2-sensing mechanism on surfaces of SnO_2/Pd_{atom} configuration.

of the coupling hybridization between Pd 4d orbital and O 2p orbital, it promoted the adsorption as well as dissociation of oxygen molecules on the surfaces of SnO_2/Pd_{atom}, and then the yielded O^- ions will spill over to the SnO_2–Pd_{atom} interface. Such a process enabled an increase in sensor resistance. Once such a sensor was exposed to H_2 gas, H_2 gas molecules adsorbed on the SnO_2–Pd_{atom} interface would react with O^- ions, forming water and releasing plenty of electrons as follows: $H_2 + O^- \rightarrow H_2O(gas) + e^-$. Consequently, a quantity of electrons would return into

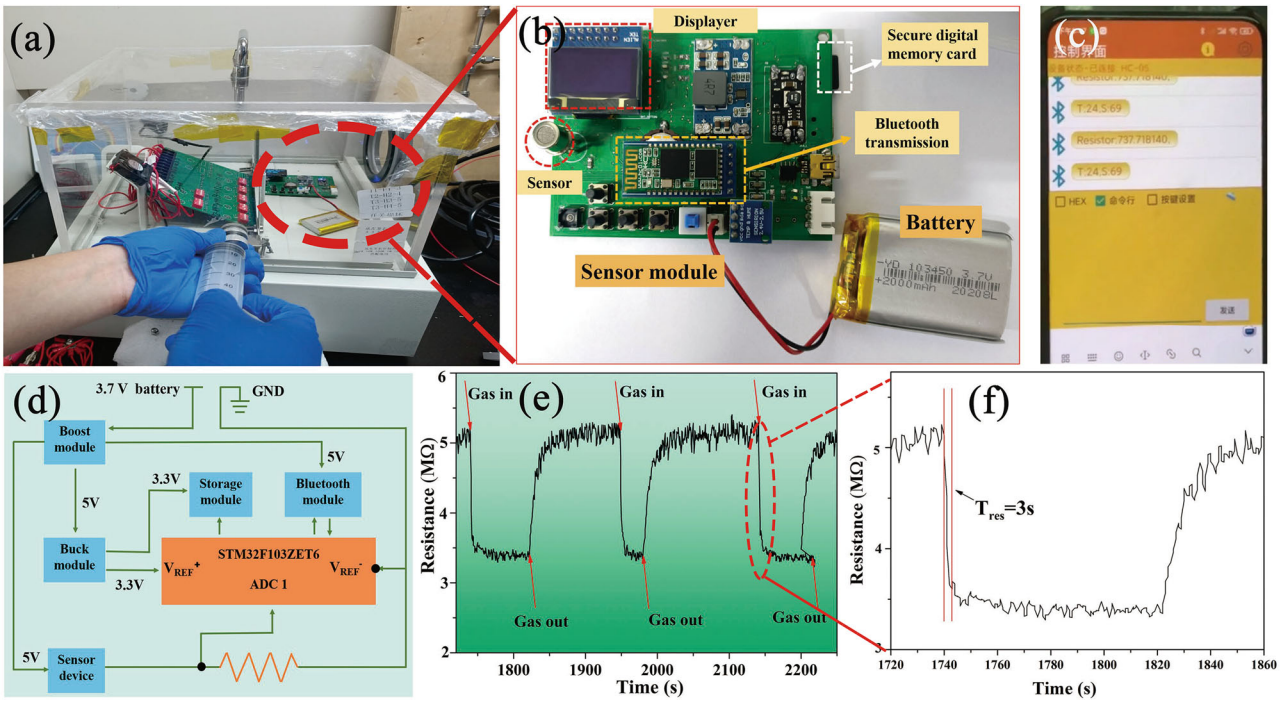

Fig. 5 | H_2-sensing module with wireless transmission function. a The real-time H_2 detection of the wireless sensing module based on SnO_2/Pd_{atom} sensor in a closed chamber. **b** Photograph of integrated wireless H_2 gas sensing module. **c** Real-time H_2-sensing data transmission showed on a mobile device. **d** Schematic circuit image of the whole wireless H_2 gas sensing module. **e** Real-time sensing result for 1 ppm H_2 gas from integrated wireless sensing module based on SnO_2/Pd_{atom} sensor, **f** the locally enlarged image of response time of SnO_2/Pd_{atom} sensor to 1 ppm H_2 in a practical test.

SnO_2/Pd_{atom} materials, lowering the resistance of sensors. Thus, the enhanced H_2-sensing properties for sensors based on SnO_2/Pd_{atom} materials were acquired.

Furthermore, to evaluate the application potential of SnO_2/Pd_{atom}-based sensors for use in real-time H_2 detection, a miniaturized the H_2-sensing module with wireless transmission function was developed (Fig. 5a, b). As shown in Fig. 5d, such a module was composed of SnO_2/Pd_{atom}-based sensors, a microcontroller unit (MCU) chip (STM32F103ZET6), a Bluetooth module, a boost and buck module, a digital memory card, an OLED display, and a 3.7 V battery. During conducting real-time H_2 detection, a certain concentration of H_2 was injected into a sealed chamber containing such H_2-sensing module (Fig. 5a), and the resistance change signal of SnO_2/Pd_{atom}-based sensors was handled via MCU and then transmitted in real time to the mobile phone control interface by Bluetooth mode (Fig. 5c). In fact, when injecting H_2 (1 ppm) three times repeatedly, variations in signal of sensor resistance (Fig. 5e) recorded in mobile phone terminal exhibited excellent repeatable H_2-sensing features with extremely fast detection speed (Fig. 5f), demonstrating its outstanding potential for application in ultrafast and highly sensitive detection for H_2 gas. Specifically, the durability of the wireless sensing module based on SnO_2/Pd_{atom} sensor under fluctuating environmental conditions was also evaluated. Primarily, the sensing module was placed in a programmable constant temperature and humidity test chamber. As shown in Supplementary Fig. 21, under the environmental temperature of 25 °C, with the change of relative humidity (RH) from 10% to 90%, the sensing module could stably collect the detection signal toward 1 ppm H_2, which validated its good moisture resistance. Moreover, the performances of such a module were also traced under various temperatures. As shown in Supplementary Fig. 22, under the RH of 45% in the environment, varying temperature from 25 °C to 60 °C, it was found that the detection signal of sensors toward 2 ppm H_2 was also stably collected by such module, and the baseline resistance of sensors collected under different ambient temperature is relatively stable (Supplementary Fig. 22a), indicating that such sensing module owned a good stability under the varying temperature.

Conclusions

Summarily, a gas sensor based on Pd SA-doped SnO_2 sensing layer was exploited to promote the ultrafast and highly sensitive detection for ppb-level H_2 gas. DFT calculations showed that the SnO_2–Pd_{atom} interface was an optimal active site, which not only strengthened the adsorption of H_2 but also promoted electron transfer from H_2 to sensing materials. Moreover, the actual sensing tests exhibited that such SnO_2/Pd_{atom} materials owned an ultrafast response speed toward H_2 (3s to 10 ppm H_2), with a detection limit of 50 ppb and superior selectivity, which was far better than those of pure SnO_2, Pd NPs, or PdO particles doped SnO_2. Significantly, using in-situ THz TDS, XPS, and DFT calculations, it demonstrated that an extra energy band that originated from Pd SAs was produced near the Fermi level in energy band structure diagrams of SnO_2/Pd_{atom} materials, and the introduction of Pd SAs greatly boosted the concentration of free carriers in SnO_2 materials. PDOS calculations further showed that the coupling hybridization between Pd 4d orbital and O 2p orbital improved the dissociation of the O=O bond of surface-adsorbed oxygen, generating more O^- ions on surfaces of SnO_2/Pd_{atom} material, as demonstrated by the XPS test. Based on theoretical calculations and experimental data, a sensing mechanism involving a spillover of O^- ions at the SnO_2–Pd_{atom} interface was proposed. Significantly, the practical detection ability of such SnO_2/Pd_{atom}-based sensors was also estimated by developing a wireless H_2-sensing module. This study provided a promising potential for achieving H_2 detection with ultrafast speed and high selectivity.

Methods

Chemicals and materials

Tin (IV) tetrachloride pentahydrate ($SnCl_4{\cdot}5H_2O$) (98%), concentrated hydrochloric acid (HCl) (36–38 wt%) purchased from Hefei baotian Science and Trade Co., Ltd. Tetraammine dichloropalladium (II) monohydrate (Pd~40.0%), sodium borohydride, ethanol (99.7%) and deionized (DI) water purchased from MACKLIN reagent. All chemicals were used as received without further purification.

Synthesis of SnO_2 nanospheres

SnO_2 nanospheres were synthesized by a modified approach in accordance with previous reports. 0.8 g $SnCl_4$ was dissolved into a 110 mL mixture, which consisted of ethanol and DI water ($v/v = 10/1$), and subsequently stirred for 10 min. Then 1.0 mL HCl was dropped into the above dispersion and stirred for 4 h. The dispersion was put into a Teflon-lined autoclave and retained heat for 12 h at 200 °C. Ultimately, the obtained products were centrifuged and washed with ethanol and DI water three times, respectively. The washed products were re-dispersed into ethanol for future use.

Synthesis of Pd SA-doped SnO_2 (SnO_2/Pd_{atom})

The SnO_2 nanospheres (200 mg) were dispersed into 100 mL of deionized water by an ultrasonic operation. Subsequently, the 0.75 mL, 1 mg/mL tetraammine dichloropalladium (II) solution was injected into the above SnO_2 dispersion, stirring continuously for 48 h. In such a study, the tetraammine dichloropalladium (II) monohydrate was chosen as the Pd source. When the tetraammine dichloropalladium (II) monohydrate was dissolved in deionized water, $[Pd(NH_3)_4]^{2+}$ cations existed in aqueous solutions. Then, the centrifugation and washing process were carried out three times by using ethanol and DI water, respectively. The washed samples were dried at 60 °C and then calcined in air at 800 °C with a heating rate of 10 °C/min.

In addition, PdO particles or Pd NPs modified SnO_2 samples were also fabricated by changing the amount of tetraammine dichloropalladium solution.

Material characterizations

Field-emission scanning electron microscopy (FE-SEM), field-emission TEM, high-resolution TEM (HR-TEM), and EDS mapping are utilized to evaluate the configuration and features of as-synthesized samples. The crystalline phase and components of the samples were analyzed via the XRD instrument. XPS was carried out via a PREVAC system. ICP-MS tests were carried out in an ICAP Qc apparatus. SAC-TEM (Titan ETEM Themis G2 300, 300 KV) is used to observe atomically dispersed Pd atoms.

XAS measurement

Pd K-edge XAS were conducted with a Si (311) crystal monochromator at the 1W1B beamline of the Beijing Synchrotron Radiation Facility (BSRF, Beijing, China). The XAFS spectra were recorded at room temperature using a 4-channel Silicon Drift Detector (SDD) Bruker 5040. The XAFS spectra of these standard samples were recorded in transmission mode. The electron beam energy of the storage ring was 2.5 GeV, and the maximum stored current was ≈200 mA. For all samples, EXAFS spectra were recorded in transmission mode. The EXAFS oscillations were extracted from the normalized XAS spectra by subtracting the atomic background using a cubic spline fit to k^2-weighted data, where k is the photoelectron wave number. The $\chi(k)$ functions were then Fourier transformed into R-space. The spectra were processed and analyzed by the software code Athena.

THz TDS measurement

The home-built terahertz time domain spectroscopy is based on an amplified Ti:sapphire laser system (Coherent Legend), delivering femtosecond pulses with 800 nm wavelength, 1000 Hz repetition rate, and 45 fs durations. A beamsplitter was used to divide the pulse into two parts for sampling and generating the THz pulses via two [110] ZnTe crystal. The optical chopper was placed in the terahertz generation path for the detection of the THz electric field waveform. All the experiments were performed under a dry nitrogen purge at room temperature.

Raman spectrum measurement

The Raman Spectrum measurements were performed on a confocal Raman spectrometer (RENISHAW Invia). The SERS measurements employed an excitation wavelength of 785 nm, a laser power of 1 mW, an integration time of 5 s, and a laser spot size of ≈2 μm. The detailed testing process is as follows: The in-situ testing chamber with sensing module was developed, and the H_2 with a given concentration was injected into such a chamber. The removal of H_2 was achieved by opening the gas outlet, allowing the H_2 to quickly diffuse out into a well-ventilated space.

Theoretical calculation method

We have employed the VASP[55,56] to perform all the spin-polarized density functional theory (DFT) calculations within the generalized gradient approximation (GGA) using the Perdew-Burke-Ernzerhof (PBE)[57] formulation. We have chosen the projected augmented wave (PAW) potentials[58] to describe the ionic cores. Take valence electrons into account using a plane wave basis set with a kinetic energy cutoff of 450 eV. Partial occupancies of the Kohn–Sham orbitals were allowed using the Gaussian smearing method and a width of 0.05 eV. The electronic energy was considered self-consistent when the energy change was smaller than 10^{-5} eV. A geometry optimization was considered convergent when the energy change was smaller than 0.03 eV/Å. The Brillouin zone is sampled with $3 \times 3 \times 1$ Monkhorst–Pack[59]. Adsorption energy can be calculated using DFT energy, so that $E_{ads} = E_{surface\_mol} - E_{surface} - E_{mol}$, where $E_{surface\_mol}$ is the energy adsorbed on the surface by molecules, $E_{surface}$ is the energy of the defective surface, and E_{mol} is the energy of the adsorbed molecule.

Gas sensing testing process

The as-prepared samples were put primarily into absolute ethanol to form a uniform dispersion, followed by brushing them on a plate electrode to obtain gas sensors. Whereafter, the aging process for gas sensors was continuously performed at 150 °C for five days. The gas sensors were placed in a static testing system with a DC multimeter power supply and a 20 L testing chamber for gas sensing measurement. During the whole testing process, the target gas was injected into the testing chamber, and the actual concentration of the injected target gas was determined based on the equation. $V_{injection} \times 20{,}000\ \text{ppm} = X\ \text{ppm} \times 20\ \text{L}$, where the X and $V_{injection}$ represent the actual concentration and volume of injected target gas in the chamber, respectively. 20,000 ppm is the original gas concentration in the gas cylinder. Then, the gas sensing measurements were implemented at the relative humidity of 45% and the ambient temperature of 25 °C. The gas response was defined as R_{air}/R_{gas}, where R_{air} and R_{gas} denote the resistance of gas sensors in air and target gas, respectively. Additionally, the response/recovery time is based on the definition of time that the resistance value of sensors reaches 90% of the final equilibrium value.

Data availability

The data that support the findings of this study are available from the corresponding author upon reasonable request.

Received: 21 November 2024; Accepted: 24 June 2025;
Published online: 04 July 2025

References

1. Darmadi, I., Nugroho, F. A. A. & Langhammer, C. High-performance nanostructured palladium-based hydrogen sensors-current limitations and strategies for their mitigation. *ACS Sens.* **5**, 3306–3327 (2020).
2. Jo, M.-S. et al. Ultrafast (~0.6 s), robust, and highly linear hydrogen detection up to 10% using fully suspended pure Pd nanowire. *ACS Nano* **17**, 23649–23658 (2023).
3. Lee, H.-S., Kim, J., Moon, H. & Lee, W. Hydrogen gas sensors using palladium nanogaps on an elastomeric substrate. *Adv. Mater.* **33**, 2005929 (2021).
4. Kumar, V. et al. Experimental and theoretical studies of sputter deposited pure SnO_2 thin films for high selective and humidity-tolerant H_2 gas sensor. *J. Mater. Sci. Mater. El* **35**, 1957 (2024).
5. Koo, W.-T. et al. Chemiresistive hydrogen sensors: fundamentals, recent advances, and challenges. *ACS Nano* **14**, 14284–14322 (2020).
6. Gautam, D. et al. Highly selective and extensive range room temperature hydrogen gas sensor based on Pd-Mg alloy thin films. *Ieee. Sens. J.* **24**, 40423–40430 (2024).

7. Sanger, A., Kumar, A., Kumar, A. & Chandra, R. Highly sensitive and selective hydrogen gas sensor using sputtered grown Pd decorated MnO_2 nanowalls. *Sens. Actuators B Chem.* **234**, 8–14 (2016).
8. Kim, K.-H. et al. Long-term reliable wireless H_2 gas sensor via repeatable thermal refreshing of palladium nanowire. *Nat. Commun.* **15**, 8761 (2024).
9. Li, J. et al. Essential role of lattice oxygen in hydrogen sensing reaction. *Nat. Commun.* **15**, 2998 (2024).
10. Gautam, D. et al. Recent developments in SnO_2 nanostructures inspired hydrogen gas sensors. *Int. J. Hydrog. Energ.* **81**, 313–345 (2024).
11. Zhang, H., Zhang, Z., Li, Z., Han, H., Song, W. & Yi, J. A chemiresistive-potentiometric multivariate sensor for discriminative gas detection. *Nat. Commun.* **14**, 3495 (2023).
12. van den Broek, J., Abegg, S., Pratsinis, S. E. & Güntner, A. T. Highly selective detection of methanol over ethanol by a handheld gas sensor. *Nat. Commun.* **10**, 4220 (2019).
13. Penner, R. M. A nose for hydrogen gas: fast, sensitive H_2 sensors using electrodeposited nanomaterials. *Acc. Chem. Res.* **50**, 1902–1910 (2017).
14. Kumar, A., Kumar, A. & Chandra, R. Fabrication of porous silicon filled Pd/SiC nanocauliflower thin films for high performance H_2 gas sensor. *Sens. Actuators B Chem.* **264**, 10–19 (2018).
15. Gautam, Y. K., Sanger, A., Kumar, A. & Chandra, R. A room temperature hydrogen sensor based on Pd-Mg alloy and multilayers prepared by magnetron sputtering. *Int. J. Hydrog. Energ.* **40**, 15549–15555 (2015).
16. Li, G. et al. Pd nanoparticles decorated SnO_2 ultrathin nanosheets for highly sensitive H_2 sensor: experimental and theoretical studies. *Int. J. Hydrog. Energ.* **50**, 761–771 (2024).
17. Lu, S. et al. Sensitive H_2 gas sensors based on SnO_2 nanowires. *Sens. Actuators B Chem.* **345**, 130334 (2021).
18. Roldan Cuenya, B. Metal nanoparticle catalysts beginning to shape-up. *Acc. Chem. Res.* **46**, 1682–1691 (2013).
19. Liu, L. & Corma, A. Metal catalysts for heterogeneous catalysis: from single atoms to nanoclusters and nanoparticles. *Chem. Rev.* **118**, 4981–5079 (2018).
20. Liu, B., Zhang, L., Luo, Y., Gao, L. & Duan, G. The dehydrogenation of H-S bond into sulfur species on supported Pd single atoms allows highly selective and sensitive hydrogen sulfide detection. *Small* **17**, 2105643 (2021).
21. Chu, T., Rong, C., Zhou, L., Mao, X., Zhang, B. & Xuan, F. Progress and perspectives of single-atom catalysts for gas sensing. *Adv. Mater.* **35**, 2206783 (2023).
22. Giulimondi, V., Mitchell, S. & Pérez-Ramírez, J. Challenges and opportunities in engineering the electronic structure of single-atom catalysts. *Acs. Catal.* **13**, 2981–2997 (2023).
23. Liang, X., Fu, N., Yao, S., Li, Z. & Li, Y. The progress and outlook of metal single-atom-site catalysis. *J. Am. Chem. Soc.* **144**, 18155–18174 (2022).
24. Ozin, G. Single atom catalysis-Back to the future. *Matter.* **7**, 2354–2348 (2024).
25. Wang, P. et al. Single-atom Cu stabilized on ultrathin $WO_{2.72}$ nanowire for highly selective and ultrasensitive ppb-level toluene detection. *Adv. Sci.* **10**, 2302778 (2023).
26. Liu, P. et al. Synergy between palladium single atoms and nanoparticles via hydrogen spillover for enhancing CO_2 photoreduction to CH_4. *Adv. Mater.* **34**, 2200057 (2022).
27. Du, F. et al. Pd-single-atom coordinated biocatalysts for chem-/sono-/photo-trimodal tumor therapies. *Adv. Mater.* **33**, 2101095 (2021).
28. Li, G., Cheng, Z., Xiang, Q., Yan, L., Wang, X. & Xu, J. Bimetal PdAu decorated SnO_2 nanosheets based gas sensor with temperature-dependent dual selectivity for detecting formaldehyde and acetone. *Sens. Actuators B Chem.* **283**, 590–601 (2019).
29. Liu, B., Li, K., Luo, Y., Gao, L. & Duan, G. Sulfur spillover driven by charge transfer between AuPd alloys and SnO_2 allows high selectivity for dimethyl disulfide gas sensing. *Chem. Eng. J.* **420**, 129881 (2021).
30. Veziroglu, S. et al. PdO nanoparticles decorated TiO_2 film with enhanced photocatalytic and self-cleaning properties. *Mater. Today Chem.* **16**, 100251 (2020).
31. Yang, W. et al. Boosting the activity of Pd single atoms by tuning their local environment on ceria for methane combustion. *Angew. Chem. Int. Ed.* **62**, e202217323 (2023).
32. Chen, L. et al. Dynamic evolution of palladium single atoms on anatase titania support determines the reverse water-gas shift activity. *J. Am. Chem. Soc.* **145**, 10847–10860 (2023).
33. Muravev, V. et al. Interface dynamics of Pd-CeO_2 single-atom catalysts during CO oxidation. *Nat. Catal.* **4**, 469–478 (2021).
34. Degler, D., Weimar, U. & Barsan, N. Current understanding of the fundamental mechanisms of doped and loaded semiconducting metal-oxide-based gas sensing materials. *ACS Sens.* **4**, 2228–2249 (2019).
35. Schmitt, E. A., Krott, M., Epifani, M., Suematsu, K., Weimar, U. & Barsan, N. Volatile organic compound sensing with WO_3-based gas sensors: surface chemistry basics. *J. Phys. Chem. C.* **128**, 1633–1643 (2024).
36. Sun, Y. & Wang, H. H. High-performance, flexible hydrogen sensors that use carbon nanotubes decorated with palladium nanoparticles. *Adv. Mater.* **19**, 2818–2823 (2007).
37. Großmann, K., Wicker, S., Weimar, U. & Barsan, N. Impact of Pt additives on the surface reactions between SnO_2, water vapour, CO and H_2; an operando investigation. *Phys. Chem. Chem. Phys.* **15**, 19151–19158 (2013).
38. Pohle, R., Fleischer, M. & Meixner, H. In situ infrared emission spectroscopic study of the adsorption of H_2O and hydrogen-containing gases on Ga_2O_3 gas sensors. *Sens. Actuators B Chem.* **68**, 151–156 (2000).
39. Gao, Z. et al. A facile PDMS coating approach to room-temperature gas sensors with high humidity resistance and long-term stability. *Sens. Actuators B Chem.* **325**, 128810 (2020).
40. Tan, Y. et al. Improving anti-humidity property of a SnO_2-based chemiresistive hydrogen sensor by a breathable and hydrophobic fluoropolymer coating. *Langmuir* **38**, 13833–13840 (2022).
41. Liu, Y. et al. Wide-concentration-range hydrogen sensing using palladium-loaded SnO_2 nanoparticle films and understanding of hydrogen concentration-dependent sensing mechanism. *Int. J. Hydrog. Energ.* **62**, 783–793 (2024).
42. Degler, D. et al. Gold-loaded tin dioxide gas sensing materials: mechanistic insights and the role of gold dispersion. *ACS Sens.* **1**, 1322–1329 (2016).
43. Hübner, M., Koziej, D., Grunwaldt, J.-D., Weimar, U. & Barsan, N. An Au clusters related spill-over sensitization mechanism in SnO_2-based gas sensors identified by operando HERFD-XAS, work function changes, DC resistance and catalytic conversion studies. *Phys. Chem. Chem. Phys.* **14**, 13249–13254 (2012).
44. Degler, D. et al. Platinum loaded tin dioxide: a model system for unravelling the interplay between heterogeneous catalysis and gas sensing. *J. Mater. Chem. A.* **6**, 2034–2046 (2018).
45. Staerz, A., Weimar, U. & Barsan, N. Current state of knowledge on the metal oxide based gas sensing mechanism. *Sens. Actuators B Chem.* **358**, 131531 (2022).
46. Myasnikov, E. N. & Myasnikova, A. E. Band theory of semiconductors and autolocalization of electrons. *Phys. Lett. A.* **286**, 210–216 (2001).
47. Liu, L. Z., Li, T. H., Wu, X. L., Shen, J. C. & Chu, P. K. Identification of oxygen vacancy types from Raman spectra of SnO_2 nanocrystals. *J. Raman Spectrosc.* **43**, 1423–1426 (2012).
48. Ozbakir, Y. et al. Exploring characteristics of palladium-loaded tin (IV) oxide nanohybrids towards chemiresistive gas sensing. *Appl. Surf. Sci.* **690**, 162530 (2025).
49. Zhang, H. et al. In situ dynamic tracking of heterogeneous nanocatalytic processes by shell-isolated nanoparticle-enhanced Raman spectroscopy. *Nat. Commun.* **8**, 15447 (2017).

50. Liu, Y. et al. Fluorination of covalent organic framework reinforcing the confinement of Pd nanoclusters enhances hydrogen peroxide photosynthesis. *J. Am. Chem. Soc.* **145**, 19877–19884 (2023).
51. Wang, X. et al. Engineering 3d-2p-4f gradient orbital coupling to enhance electrocatalytic oxygen reduction. *Adv. Mater.* **34**, 2206540 (2022).
52. Bilal, M. et al. Optoelectronic properties of monolayer hexagonal boron nitride on different substrates measured by terahertz time-domain spectroscopy. *Nanomaterials* **10**, 762 (2020).
53. Němec, H., Kužel, P. & Sundström, V. Far-infrared response of free charge carriers localized in semiconductor nanoparticles. *Phys. Rev. B.* **79**, 1153091–11153097 (2009).
54. Franke, M. E., Koplin, T. J. & Simon, U. Metal and metal oxide nanoparticles in chemiresistors: does the nanoscale matter?. *Small* **2**, 36–50 (2006).
55. Kresse, G. et al. Efficiency of ab-initio total energy calculations for metals and semiconductors using a plane-wave basis set. *Comp. Mater. Sci.* **6**, 15–50 (1996).
56. Kresse, G. et al. Efficient iterative schemes for ab initio total-energy calculations using a plane-wave basis set. *Phys. Rev. B* **54**, 11169–11186 (1996).
57. Perdew, J. P. et al. Generalized gradient approximation made simple. *Phys. Rev. Lett.* **77**, 3865–3868 (1996).
58. Kresse, G. & Joubert, D. From ultrasoft pseudopotentials to the projector augmented-wave method. *Phys. Rev. B* **59**, 1758–1775 (1999).
59. Monkhorst, H. J. & Pack, J. D. Special points for Brillouin-zone integrations. *Phys. Rev. B* **13**, 5188–5192 (1976).

Acknowledgements

The authors acknowledge the support from the National Natural Science Foundation of China (Grant No. 62471172 and 62001178). Herein, the authors are very grateful to Fuhai Su and Jin Yang for helping us with THz TDS measurements.

Author contributions

Yunxiao Qian, Guorui Zhao and Changmin Zhang contributed equally to this work. Bo Liu directed this study. Yunxiao Qian performed the preparation, characterization, data analysis, and sensing test of Pd SA-doped SnO_2 materials, Guorui Zhao and Yuanyuan Luo conducted DFT calculations and analysis, and Changmin Zhang developed a wireless H_2-sensing module based on the SnO_2/Pd_{atom} sensor. Shengjie Yin, Junwei Chen, Zhengfeng Huang, and Guotao Duan contributed the analysis and discussion of the sensing mechanism. Bo Liu supervised this study and wrote the manuscript. All the authors discussed and reviewed the final manuscript.

Competing interests

The authors declare no competing interests.

Additional information

Supplementary information The online version contains supplementary material available at https://doi.org/10.1038/s43246-025-00865-5.

Correspondence and requests for materials should be addressed to Bo Liu.

Peer review information *Communications Materials* thanks Ashwani Kumar, Bo Xie, and the other anonymous reviewer(s) for their contribution to the peer review of this work. Primary Handling Editors: Ruben Rizo and Jet-Sing Lee. [A peer review file is available].